Materials Horizons

ROYAL SOCIETY OF CHEMISTRY

COMMUNICATION

View Article Online
View Journal



Cite this: DOI: 10.1039/d5mh02009c

Received 23rd October 2025,
Accepted 12th January 2026

DOI: 10.1039/d5mh02009c

rsc.li/materials-horizons

# A high-entropy gradient filler metal enables high-strength joints of $Ti_2AlNb$ and GH4169 alloys

Yinchen Wang,† Zhijie Ding,† Bin Wang, Zhenyang Zhang, Zhiwei Qin,* Jia Yao, Yu Sun, Fengyun Yu, Honggang Dong and Peng Li *

**Vacuum brazing with an innovative filler alloy is critical for manufacturing high-precision aerospace components requiring exceptional comprehensive performance, yet achieving superior strength in $Ti_2AlNb$/GH4169 brazed joints remains challenging. This study proposes a $(TiZrHf)_{50}(NiCu)_{45}Al_5/(TiZrHf)_{30}(NiCu)_{65}Al_5$ high-entropy gradient filler metal (HGFM) to join the $Ti_2AlNb$ alloy and the GH4169 superalloy, which relieved the stress concentration and elevated microstructure stability, achieving a maximum shear strength of 335 MPa. The lower thermodynamic inclination and high entropy characteristics synergistically contributed to the solid solution mainly composed of $(Ni,Cr,Fe)_{ss}$ and $(Ni,Cu,Fe,Cr)_{ss}$ phases, replacing the intermetallic compounds dominated by $(Ti,Zr,Hf)(Ni,Cu)_3$ and $(Ti,Zr,Hf)_2(Ni,Cu)$ phases. The corresponding lattice misfits between $(Ni,Cr,Fe)_{ss}$ and $(Ni,Cu,Fe,Cr)_{ss}$ phases were 3.72%, 13.24% and 20.14%, which enabled coherent and semi-coherent relationships, facilitating the dynamic equilibrium of dislocation motion without termination. A higher activation energy at the interface (393 kJ $mol^{-1}$) indicated that slow atomic diffusion controlled the excessive reaction at the interface. The remarkable drop in elastic modulus discrepancies in the customized solid solution region enhanced the synergistic deformation capacities, which drove the fracture locations to transform to the $Ti_2AlNb$ dissolved with Ni and Cu phases, exhibiting a more tortuous fracture path and higher fracture toughness. Molecular dynamics simulations indicated that the solid solution interface enhanced the peak tensile strength to 10.36 GPa, demonstrating favorable high-temperature stability. The current work offers a directly transferable approach for developing a tailored filler metal for other dissimilar metal systems.**

**New concepts**

This work proposes a high-entropy gradient filler metal (HGFM) to fundamentally control interfacial reactions and achieve high-strength brazing of the $Ti_2AlNb$ alloy and the GH4169 superalloy. By engineering a continuous compositional gradient between dissimilar metals, the thermodynamic inclination for brittle intermetallic formation was suppressed. Concurrently, the high-entropy characteristic promoted ductile phases to replace brittle phases, which enabled the growth of a coherent/semi-coherent solid-solution interface, facilitating the dynamic equilibrium of dislocation motion without termination and managing interfacial strain. This underlying rationale-gradient design, coupled with entropy stabilization, forms a generalizable strategy for joining other metal systems.

## 1 Introduction

The need for aeroengine key components in extreme environments has gained considerable attention for the development of lightweight brazed structures.[1,2] The $Ti_2AlNb$ alloy, noted for its low density and high specific strength,[3] presents a promising lightweight high-temperature structural material for next-generation aircraft engines, potentially superseding widely used superalloys such as GH4169.[4] Achieving a high-performance Ti–Ni brazed structure is essential to leverage their complementary properties for enhanced lightweight and high-temperature performance in aero-engines.

Direct brazing of $Ti_2AlNb$ and superalloys due to the marked divergence in physicochemical properties often results in problems such as voids, kissing bonds, and many IMCs,[5,6] which, in turn, severely degrade mechanical properties. To address these critical challenges, filler metals, including composite metallic foils and amorphous filler metals,[7] have been explored. The introduction of filler metals can promote the filling of voids and the formation of reaction layers through concentration gradients and the wetting behaviors,[8,9] thereby alleviating the above problems. Nevertheless, the limited mechanical performance of current filler alloys, especially at elevated temperatures,[10] severely restricts their widespread applications in critical turbine components. Thus, developing innovative high-performance filler metals and elucidating interfacial strengthening mechanisms in the joints are imperative for achieving high comprehensive mechanical performance.

High entropy alloys (HEAs), the sought-after metallic material with exceptional mechanical properties,[11,12] have recently

*School of Materials Science and Engineering, Dalian University of Technology, Dalian 116024, PR China. E-mail: lipeng2016@dlut.edu.cn, qinzw@dlut.edu.cn*
† These authors contributed equally to this work.

emerged as promising candidates for use as interlayers in brazing applications. The primary strengthening in HEAs was achieved by mixing multiple matrix elements.[13] High-entropy alloy filler metals facilitate interfacial solid solution (SS) formation,[14] suppress excessive substrate dissolution, and restrain elemental diffusion, thereby inhibiting the formation of brittle IMCs in brazed joints. Furthermore, gradient materials exhibit a stronger synergy in terms of strength and plasticity compared to homogeneous microstructures, due to enhanced strain accommodation capabilities and optimized stress distribution.[15,16] Inspired by the high entropy concept and gradient design, this paper is expected to develop a gradient transition HEA as an innovative filler metal for brazing the $Ti_2AlNb$ alloy and the GH4169 superalloy, which can effectively overcome the significant interfacial thermodynamic propensity that traditional fillers fail to handle, while leveraging the inherent characteristics of HEAs to significantly enhance joint performance.

In this study, we propose a tailored $(TiZrHf)_{50}(NiCu)_{45}Al_5$/$(TiZrHf)_{30}(NiCu)_{65}Al_5$ high-entropy gradient filler metal (HGFM), fundamentally controlling the interfacial reaction and achieving high-strength brazing of $Ti_2AlNb$ and GH4169 alloys. Its gradual compositional transition minimizes the thermodynamic inclination for brittle IMCs, while the high-entropy characteristic promotes the formation of coherent/semi-coherent solid-solution interfaces. Critically, such interfaces facilitate the dynamic equilibrium of dislocation motion without termination, thereby managing interfacial strain and relieving stress. This rationale of combining the compositional gradient with entropy stabilization to forge coherent, ductile interfaces presents a generalizable approach for other dissimilar metal systems.

# 2 Experimental

## 2.1 Material preparation

Fig. S12 illustrates the microstructures of the two base metals and the XRD patterns. The GH4169 alloy mainly consisted of Ni-based SS phases, while the $Ti_2AlNb$ alloy was composed of a dark grey α2 phase, a light grey O phase, and a white matrix B2 phase. The chemical compositions of the GH4169 superalloy and the $Ti_2AlNb$ alloy are shown in Table S12. The HGFM proposed in this work was based on the following rationale: key alloying elements compatible with the base metal were selected, while elements with significantly different atomic radii were introduced as the core components of the filler system. Theoretical calculations according to eqn (S4) and (S5) indicated that the $(TiZrHf)_{50}(NiCu)_{45}Al_5$/$(TiZrHf)_{30}(NiCu)_{65}Al_5$ HGFM achieved large atomic radius mismatches of 10.56 and 10.23, coupled with high-entropy characteristics of 14.27 and 13.06. Chemical potential was employed as a key thermodynamic parameter to guide the gradient design of composition, as it reflected the tendency for inter-element reactions.[17,18] Comparative calculations using eqn (S7)–(S9) demonstrated that, compared to the single $(TiZrHf)_{50}(NiCu)_{45}Al_5$ filler, the adoption of the HGFM reduced the interfacial chemical potential gradient with the GH4169 substrate by approximately 40% (the $\Delta\mu$ decreased from 9.1 kJ mol$^{-1}$ to 5.2 kJ mol$^{-1}$ at 1293 K; the $\Delta\mu$ decreased from 9.4 kJ mol$^{-1}$ to 5.3 kJ mol$^{-1}$ at 1338 K), thereby effectively suppressing excessive thermodynamic inclinations. Meanwhile, the high-entropy filler system, leveraging its high entropy and sluggish diffusion characteristics, contributed to facilitating the formation of more solid-solution structures at the interface and restraining the intensity of interfacial reactions. The raw materials (with a purity of over 99.95%) were melted at least 8–9 times using vacuum arc melting and strip casting integrated equipment (DHL-350) in a vacuum arc heating furnace to obtain alloy ingots with uniform composition. $(TiZrHf)_{30}(NiCu)_{65}Al_5$ and $(TiZrHf)_{50}$-$(NiCu)_{45}Al_5$ high-entropy amorphous brazing foils with a width of approximately 6 mm and a thickness of about 50 μm were prepared under rapid cooling using a high-speed rotating copper roller. The corresponding crystal structures and thermal behaviors are shown in Fig. 1h and g. The XRD diffraction patterns revealed broad diffuse peaks, indicating a fully amorphous structure of brazing foils. The DSC curve illustrated a decreasing trend in the melting point of the filler metal with increasing content of Zr and Hf elements.

## 2.2 Vacuum brazing

The base metals and the HGFM foils were assembled, as shown in Fig. 1d. A filler metal with higher Ti content and lower Ni content was selected for the $Ti_2AlNb$ side, while a filler metal with lower Ti content and higher Ni content was chosen for the GH4169 side. The assembled specimens were placed in a vacuum brazing furnace (ZTF2-10), and an external pressure of 20 kPa was applied to make the specimens closely fit each other, as depicted in Fig. 1b. The brazing temperature range and holding time were 1020–1080 °C and 15 min, as shown in Fig. 1c. The shear fixture shown in Fig. 1e was used to perform the shear test on the specimens on a universal tensile testing machine (DNS-100) with a shear rate of 0.5 mm min$^{-1}$. To ensure the accuracy and authenticity, at least three shear specimens were tested under each brazing condition to obtain the average value. Based on finite element analysis (FEA),[19,20] the stress field of the joints with the $(Ti,Zr,Hf)_{50}(Ni,Cu)_{45}Al_5$ filler metal and HGFM along the horizontal and vertical directions for brazed seam was simulated, as shown in Fig. 1f and g. Compared to the $(Ti,Zr,Hf)_{50}$-$(Ni,Cu)_{45}Al_5$ filler metal, the maximum residual stress value at the brazed joint decreased from 92.0 MPa to 71.5 MPa with the HGFM, consistent with the trend observed in actual stress test results. The stress test and finite element simulation details are provided in the SI. Therefore, the employment of the HGFM effectively mitigated interfacial stress concentrations, enhancing the mechanical integrity of joints.

# 3 Results and discussion

## 3.1 Microstructure of the hybrid joint with the HGFM

Fig. 2 demonstrates the interfacial microstructure of $Ti_2AlNb$/$(TiZrHf)_{50}(NiCu)_{45}Al_5$/$(TiZrHf)_{30}(NiCu)_{65}Al_5$/GH4169 joints at

 

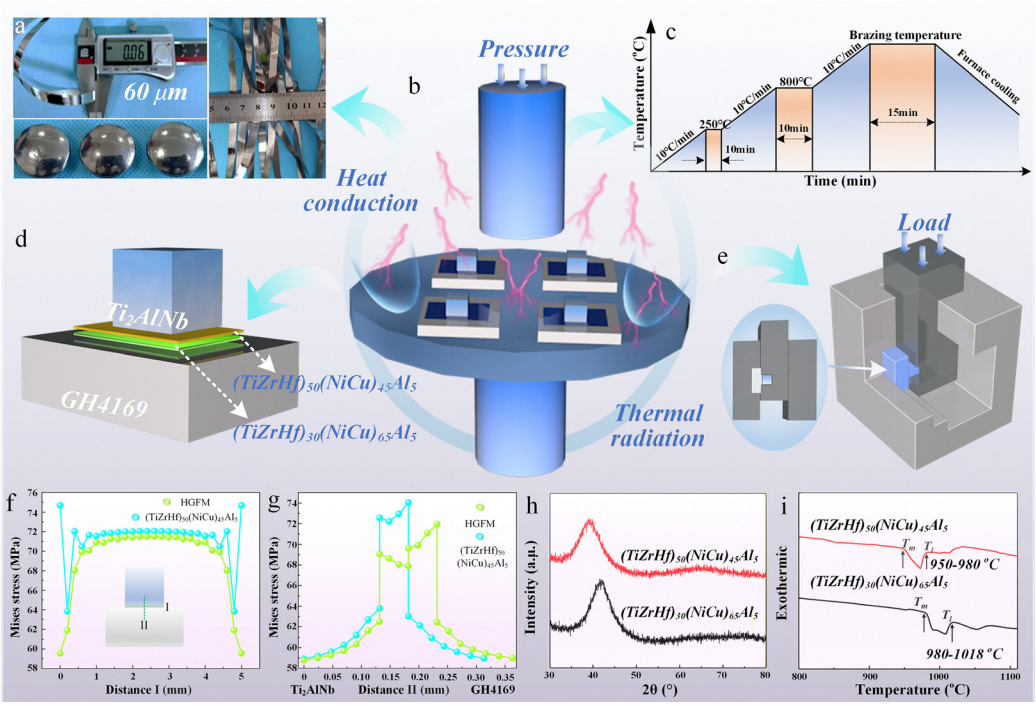


Fig. 1 Innovative design of the brazing technique with the HGFM. (a) Brazing processing curve, (b) vacuum brazing diagram, (c) alloy ingots and foils, (d) assembly of brazing specimens, (e) shear test fixture, (f) and (g) residual stress along the horizontal and vertical directions for the brazed seam, and (h) and (i) XRD patterns and DSC curves of the HGFM.

1065 °C/15 min. The brazed joint exhibited sound interfacial bonding and was free from defects, including microcracks and voids. Fig. 2c and d show significant interfacial interactions between the base metals and the HGFM, primarily involving dissolution, diffusion, and reactions. Based on the contrast of the microstructure and the elemental distribution, the brazed joint was divided into three zones: the diffusion affected zone (zone I) near the $Ti_2AlNb$ side, the central brazing zone (zone II), and the diffusion reaction zone (zone III) near the GH4169 side.

Zone I consisted of a dark grey matrix phase, denoted as phase A, and a grey phase with a wave-like morphology, labelled as phase B. The dark grey phase marked as A predominantly contained elements Ti, Al, and Nb, with trace amounts of Cu and Ni elements detected, indicating elemental diffusion from the HGFM into this region. Due to the relatively high content of Nb (a stabilizer for the β phase in titanium alloys) and the similar atomic percentage content to the $Ti_2AlNb$ alloy, combined with relevant research,[21] phase A was confirmed as the β/B2 phase. From Table S11, the elemental proportions of Ti, Al, and Nb marked as point B were close to the O phase of the $Ti_2AlNb$ substrate. In addition to Ti, Al, and Nb elements, 22.64 at% Ni and 8.60 at% Cu elements were detected, indicating the diffusion and dissolution of Ni and Cu elements. Therefore, the region marked as point B was determined as the $Ti_2AlNb$ phase with SS of Ni and Cu elements.

Zone II was predominantly composed of a bright white phase marked as point C, grey-white phases marked as points D and E, black block-like phases marked as points F and G, and a grey phase marked as point H. The bright white phase marked as point C was primarily composed of Ti, Zr, Hf, Ni, and Cu elements, with respective atomic percentages of 12.59 at%, 8.91 at%, 11.59 at%, 42.19 at%, and 21.22 at%. Based on published data[22,23] and Table S11, Zr and Hf elements were considered as the Ti-like element, while Cu was regarded as a Ni-like element. Nb also exhibited high solid solubility with Ti,[24] and Nb was classified as a Ti-like element. For point C, the total atomic percentage of Ti-site elements was ~33.1%, and that of Ni-site elements was ~63.4%. The ratio was approximately 1 : 1.92, which closely matched the stoichiometry of the $AB_2$ type Laves phase ($TiCu_2$). Thus, point C was confirmed as the $(Ti,Zr,Hf)(Ni,Cu)_2$ phase. For points D, E, F, G, and H, the A-site content ranged from 39.4% to 43.3%, and the Ti-site content ranged from 41.2% to 54.8%. The calculated ratios fell between 1 : 1 and 1 : 1.4. This indicated that these phases were AB-type compounds (TiNi-based phase). In fact, the TiNi-based phase was known to exhibit a wide solubility range towards the Ni-rich side in the ternary/quaternary systems.[25] Therefore, point D was identified as the (Ti,Zr,Nb)(Ni,Cu,Al) phase. Points E through H were confirmed as the (Ti,Zr,Nb,Hf)(Ni,Cu,Al) phase, exhibiting varying brightness due to elemental differences.

Zone III was primarily composed of three different contrast phases: a black phase denoted as phase I, a grey-white phase denoted as phase J, and a grey-black phase denoted as phase K. The J phase exhibited a higher content of Ni elements, suggesting the Ni-rich$(Ni,Cr,Fe)_{ss}$ + $(Ti,Zr)_2(Ni,Cu)$ phase, while the regions marked as points I and K were inferred as the $(Ni,Cr,Fe)_{ss}$ + $(Ti,Zr)_2(Ni,Cu)$ phase. To verify the phases formed in the brazing

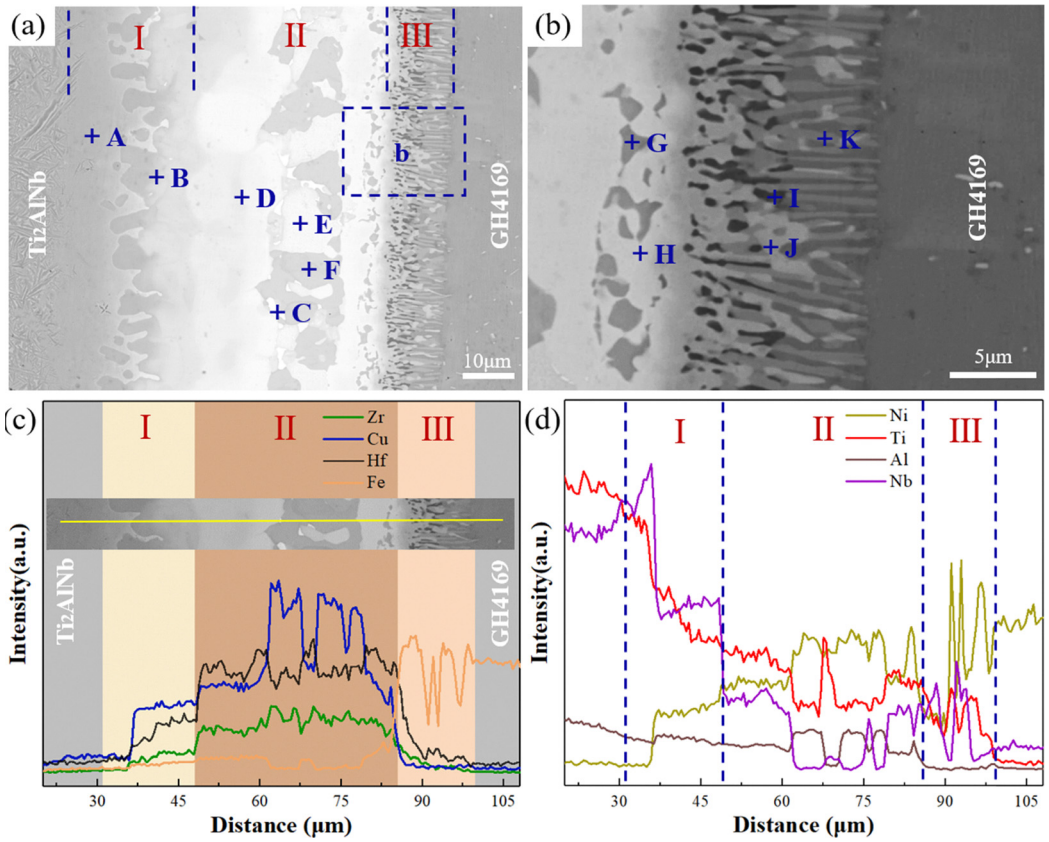


Fig. 2 Microstructures of joints brazed at 1065 °C for 15 min with the HGFM. (a) Typical interfacial microstructure, (b) enlarged image of (a), and (c) and (d) elemental distribution across joints.

seam, XRD phase analysis was conducted on the fracture surface of the $Ti_2AlNb$ side, as shown in Fig. S14, further validating the phase results shown in Table S12.

The brazing temperature affected the extent of atomic self-diffusion and mutual diffusion between the base metals and the HGFM, which is manifested thermodynamically by different reaction products at the interface and kinetically by variations in the dissolution rate of the base metal and the thickness of the reaction layer formed.[26] From the thermodynamic perspective of microstructural evolution depicted in Fig. S1–S3, with the increase in brazing temperature, the bright white phase (Ti,Zr,Hf)(Ni,Cu) and black phase $Al(Ti,Zr)(Ni,Cu)_2$ in the central interfacial region gradually transformed into the grey-white phase (Ti,Zr,Hf)(Ni,Cu,Al), exhibiting a more uniform phase distribution. From the kinetic perspective, the larger atomic size discrepancies within the HGFM itself led to severe lattice distortion and fluctuating lattice potential energy distributions.[27,28] It significantly increased the energy barriers for atomic leaps, thereby markedly reducing atomic mobility and exhibiting a slow diffusion nature. A direct comparison between joints fabricated using the conventional filler metal[29] and the HGFM is presented in Fig. S6. The calculated activation energy for interfacial layer growth increased from 224 kJ $mol^{-1}$ for the conventional filler to 393 kJ $mol^{-1}$ for the HGFM. This substantial increase confirmed a pronounced kinetic limitation, manifesting as slowed interfacial evolution and validating the efficacy of our filler design in modulating growth dynamics, mitigating over-reaction, and reducing the propensity for extensive IMC formation. At a brazing temperature of 1080 °C, the $Ti_2AlNb$ substrate underwent phase transformation and significant dissolution, resulting in a remarkable increase in the corresponding reaction layer thickness. In fact, it was a manifestation of non-equilibrium dissolution and the Kirkendall effect at high temperatures.[30] Due to the inherent hysteresis diffusion effect of the HGFM, the diffusion rate of filler elements toward the $Ti_2AlNb$ base metal side was relatively slow. At an elevated temperature of 1080 °C, the $Ti_2AlNb$ base metal underwent intense dissolution, resulting in a relatively rapid diffusion rate of Ti, Al, and Nb atoms toward the liquid phase/brazing joint. Due to the significantly greater atomic flux flowing out of the base metal than into it,[31] many lattice vacancies remained at the $Ti_2AlNb$ side interface. The enhanced vacancy densities enabled diffused atoms to easily overcome activation energy barriers, resulting in rapid growth of the interface thickness, consistent with the perspective proposed by Li *et al.*[32]

### 3.2 Interfacial crystal structure of the hybrid joint

Considering that zone II–III interfacial regions were the typical regions of joints, the corresponding compositional variation and crystal structures from 1020 °C to 1065 °C were analysed, as shown in Fig. 3 and 4. Fig. S16a shows the point analysis

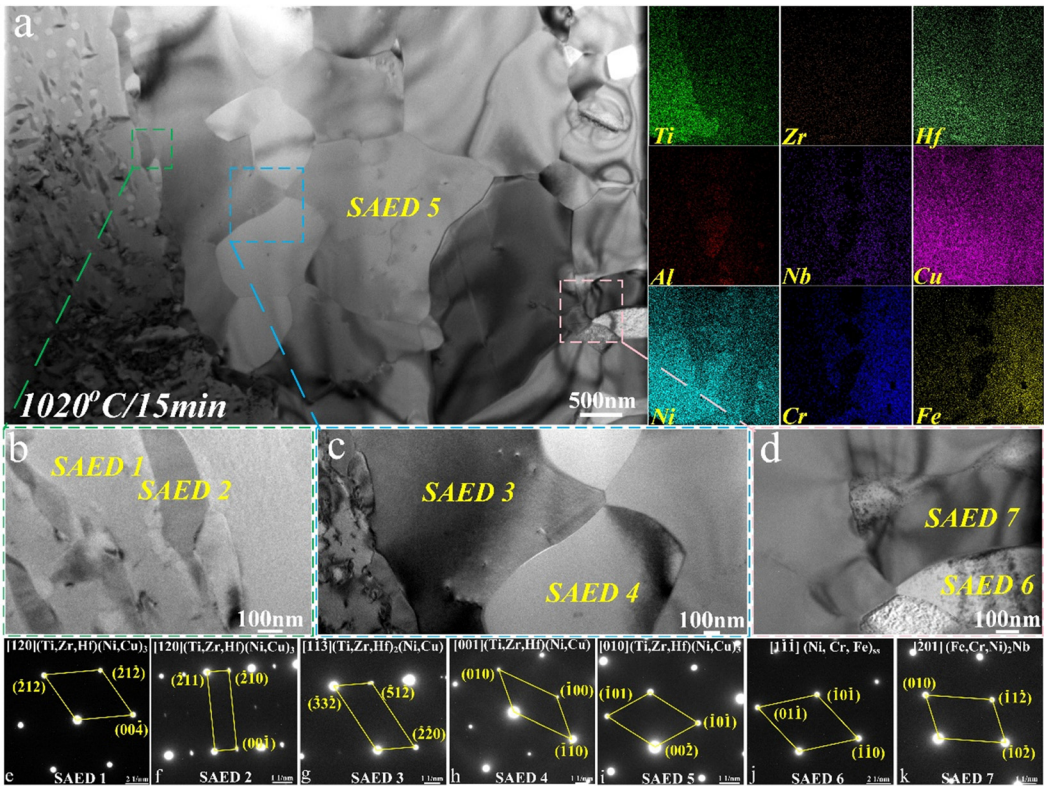


Fig. 3 TEM characterization of the zone III interface of joints brazed at 1020 °C with the HGFM. (a) Bright-field image and TEM-EDS mapping, (b)–(d) the magnified bright-field image in (a) and (e)–(k) SAED patterns corresponding to the marked locations in (a)–(d).

locations within the interfacial region at a brazing temperature of 1020 °C, and the corresponding results are presented in Table S8. Based on relevant works,[33,34] the $\Omega$ parameter could be employed to evaluate thermodynamic tendencies, as shown in eqn (1). When $\Omega$ was less than 1.1, the thermodynamic tendency was primarily driven by enthalpy. When $\Omega$ exceeded 1.1, the thermodynamic tendency was predominantly driven by entropy,

$$\Omega = T\Delta S_{\mathrm{mix}}/|\Delta H_{\mathrm{mix}}| \quad (1)$$

where $\Delta H_{\mathrm{mix}}$ and $\Delta S_{\mathrm{mix}}$ are the mixing enthalpy and mixing enthalpy between the $i$-th and $j$-th elements, while $R$ is the universal gas constant and equivalent to 8.314 J $K^{-1}$ $mol^{-1}$. Calculations of eqn (1) revealed that $\Omega$ values from point 1 to point 3 in the region were 0.59, 0.71, and 0.86, indicating a thermodynamic state driven by enthalpy. The bright-field image in Fig. 3a reveals that the left side of the interface primarily consisted of dark grey acicular phases and a grey matrix phase at 1020 °C. The central regions consisted of coarse grains, while the right-side regions were composed of fine columnar grains. As shown in the TEM-EDS image in Fig. 3a, the left region exhibited aggregation of Ti, Ni, and Cu elements, while the central and right regions were mainly characterized by the distribution of Zr, Hf, Ni, Cu, and Cr, Nb elements, respectively. Upon diffraction calibration, the selected area electron diffraction (SAED) 1 pattern was determined as the $(Ti,Zr,Hf)(Ni,Cu)_3$ phase, consistent with the SAED 2 pattern. The central regions corresponding to the SAED 3–5 patterns were calibrated as the $(Ti,Zr,Hf)(Ni, Cu)_{3[1-1-3]}$, $(Ti,Zr,Hf)(Ni, Cu)_{3[001]}$ and $(Ti,Zr,Hf)(Ni,Cu)_{3[010]}$ phases. The left regions were determined to be mixed regions of $(Ni,Cr,Fe)_{ss[1-1-1]}$ and $(Fe,Cr,Ni)_2Nb_{[-201]}$ phases.

When the brazing temperature increased, a significant change appeared in the interfacial area of joints, as shown in Fig. 4, and the main elements were distributed in a mixed condition. Fig. S16b illustrates the point analysis locations within the interfacial region at a brazing temperature of 1065 °C, and the results are summarized in Table S9. Calculations revealed that the $\Omega$ values for points 1 to 3 in Fig. S16b were 2.36, 1.84, and 1.15, suggesting an enthalpy-driven behavior. The SAED 1–3 patterns in the left regions were identified as the $(Ti,Zr,Hf)_2(Ni,Cu)_{[-49-10]}$, $(Ni,Cu,Fe,Cr)_{ss[010]}$ and $(Ti,Zr,Hf)_7(Ni,Cu)_{10[-52-6]}$ phases. The central regions showed a remarkable enrichment of the Cr element, as indicated by the SAED 4, 7–9 patterns (Fig. 4 and S8). The miller indices of the $(Ni,Cr,Fe)_{ss}$ phase in the SAED 4 pattern were calculated as $(\bar{1}\bar{1}0)$, $(\bar{1}0\bar{1})$ and $(01\bar{1})$, with the crystal band zone of $[1\bar{1}\bar{1}]$. Furthermore, the regions where the SAED 9 pattern was located represent the main grey phase in the central regions, which was confirmed as the $(Ni,Cu,Fe,Cr)_{ss[0-1-1]}$ phase with a hexagonal structure, containing $(\bar{1}00)$, $(\bar{1}1\bar{1})$ and $(0\bar{1}\bar{1})$ miller indices. As shown in the right regions of Fig. 4c, the SAED 5 and 6 patterns were identified as the $(Ni,Cr,Fe)_{ss[001]}$ and the $(Ni,Cu,Fe,Cr)_{ss[010]}$ phases, respectively.

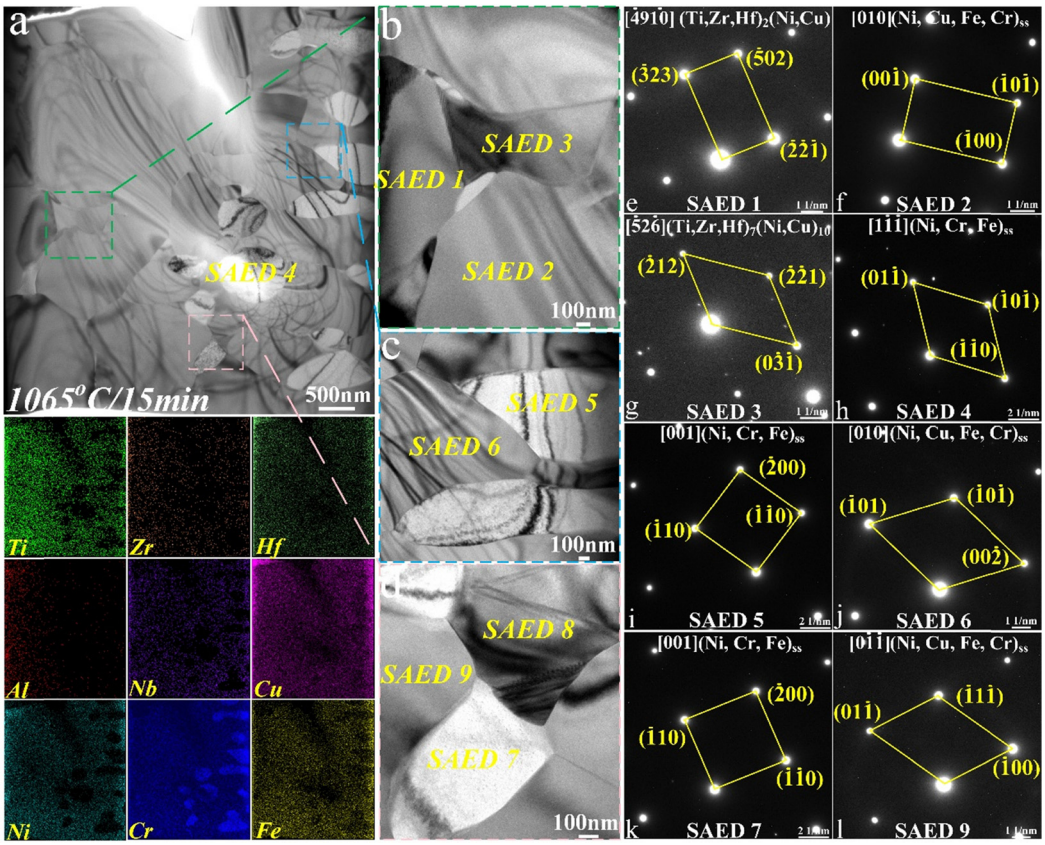


Fig. 4 TEM characterization of the zone III interface of joints brazed at 1065 °C with the HGFM. (a) Bright-field image and TEM-EDS mapping, (b)–(d) the magnified bright-field image in (a) and (e)–(l) SAED patterns corresponding to the marked locations in (a)–(d).

Overall, *via* the design of HGFM and the regulation of brazing temperature, the $\Omega$ value in the II–III interfacial regions shifted from less than 1.1 to greater than 1.1, accompanied by a transition in the lattice structures, exhibiting a mixed distribution dominated by $(Ni,Cr,Fe)_{ss}$ and $(Ni,Cu,Fe,Cr)_{ss}$ phases. This suggested that the HGFM design effectively leveraged its high-entropy characteristics, transforming the enthalpy-driven thermodynamic tendency into an entropy-driven one, thereby promoting a distribution dominated by SS at the interface.

### 3.3 Strengthened solid solution interface of the hybrid joint with the HGFM

Given that the interface was prone to the stress concentration, crack initiation and propagation, this study further investigated the lattice misfit relationship and strain distribution at the typical interface of joints brazed at 1020 °C and 1065 °C. As shown in the magnified bright-field images in Fig. 5 and S9, the interfacial regions of zone III were studied. Based on the region marked by the blue dashed line in Fig. 5a, Fig. 5d presents the high-resolution transmission electron microscopy (HRTEM) image of the $(Ti,Zr,Hf)_2(Ni,Cu)$/(Ti,Zr,Hf)(Ni,Cu) interface. Upon fast Fourier transform (FFT) and inverse fast Fourier transform (IFFT) on the interface, the lattice reconstruction image was obtained. The atomic arrangements perpendicular to the interface suggested that $(Ti,Zr,Hf)_2(Ni,Cu)$ (yellow atoms) and (Ti,Zr,Hf)(Ni,Cu) (blue atoms) presented a non-occupied occupation state at the interface, proving a non-coherent interface. To quantify this characteristic, the lattice fringe width images on both sides of the interface were reconstructed, as depicted in Fig. 5e. The lattice fringe widths of the $(Ti,Zr,Hf)_2(Ni,Cu)_{(220)}$ and $(Ti,Zr,Hf)(Ni,Cu)_{(100)}$ phases are 4.479 Å and 3.021 Å, respectively. The calculation of lattice misfit was based on eqn (2),[35]

$$\delta^{(hkl)_1}_{(hkl)_2} = \frac{|d_1 \cos\theta - d_2|}{d_2} \times 100\% \quad (2)$$

where $(hkl)_1$ and $(hkl)_2$ are the low-index crystal planes of two phases and $d_1$ and $d_2$ are the distances of $(hkl)_1$ and $(hkl)_2$, respectively. $\theta$ is the angle between them. According to eqn (2), the lattice misfit of the $(Ti,Zr,Hf)_2(Ni,Cu)$/(Ti,Zr,Hf)(Ni,Cu) interface was 37.90%, confirming the non-coherent judgment. The strain distribution in Fig. 5f revealed that localized stresses at the interface appeared, prone to premature failure. Fig. 5g shows the high-resolution transmission electron microscopy (HRTEM) image of the $(Ti,Zr,Hf)(Ni,Cu)_3$/$(Fe,Cr,Nb)_2Nb$ interface. The lattice reconstruction image in Fig. 5h shows that the $(Ti,Zr,Hf)(Ni,Cu)_3$ phase (yellow atoms) and the $(Fe,Cr,Nb)_2Nb$ phase (blue atoms) at the interface were in a non-occupied state, suggesting an incoherent interface. By measuring the lattice fringe widths of the atoms perpendicular to both sides of the interface, the fringe widths of $(Ti,Zr,Hf)(Ni,Cu)_{3(101)}$ and

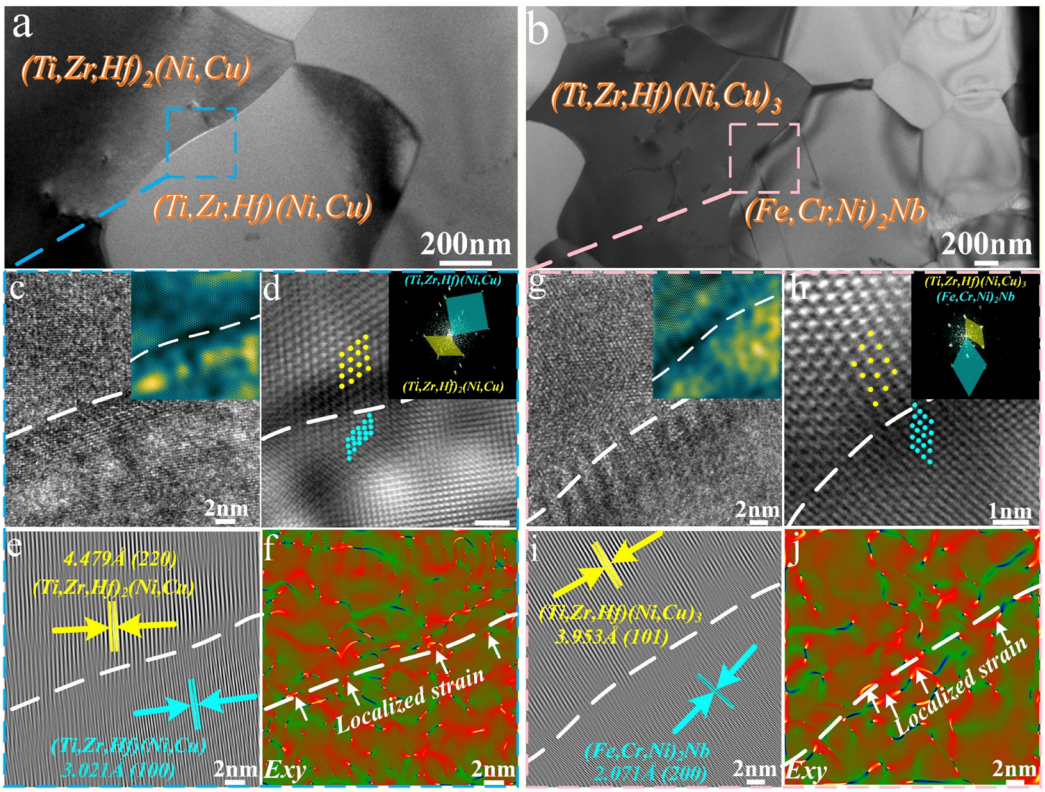


Fig. 5 Interfacial characteristics of joints brazed at 1020 °C for 15 min with the HGFM. (a) and (b) Enlarged bright field images, (c) HRTEM image and lattice distortion conditions in (a), (d) FFT and lattice reconstruction image in (c), (e) lattice fringe image in (c), (f) shear strain distributions of (c), (g) HRTEM image and lattice distortion conditions in (b), (h) FFT and lattice reconstruction image in (g), (i) lattice fringe image in (g), and (j) shear strain distributions of (g).

$(Fe,Cr,Nb)_2Nb_{(200)}$ were 3.953 Å and 2.071 Å, revealing a lattice misfit of 48.32%. The obvious localized strain at the interface (Fig. 5j) evidenced this misfit phenomenon. Similar assertions were presented by Wu *et al.*[36] Upon calibration, the fringe widths of the $(Ti,Zr,Hf)(Ni,Cu)_3$ phase (SAED 1 pattern) and the $(Ti,Zr,Hf)(Ni,Cu)_3$ phase (SAED 2 pattern) in Fig. S9(a)–(d) were determined to be 2.131 Å and 2.494 Å, respectively. The fringe widths of the $(Cr,Fe,Ni)_{ss}$ phase (SAED 6 pattern) and the $(Fe,Cr,Ni)_{ss}Nb$ phase (SAED 7 pattern) in Fig. S9(e)–(h) were 2.043 Å and 2.846 Å, respectively. Calculations *via* eqn (2) revealed lattice misfits of 25.16% and 33.23% for the $(Ti,Zr,Hf)(Ni,Cu)_3/(Ti,Zr,Hf)(Ni,Cu)_3$ interface and the $(Cr,Fe,Ni)_{ss}/(Fe,Cr,Ni)_{ss}Nb$ interface, respectively, both exhibiting incoherent configurations. The statistical results for the corresponding interfacial relationships are shown in Table S5. Therefore, the primary interfaces of joints brazed at 1020 °C were all in a non-occupied state, manifesting an incoherent interface with higher strain energies. The evident strain localization at the interface indicated that the non-coherent IMC interface state exhibited a strengthening effect achieved through the accumulation of mobile dislocations at the interface (Orowan mechanism[37,38]).

Considering that the interface of joints brazed at 1065 °C are characterized by $(Ni,Cr,Fe)_{ss}$ and $(Ni,Cu,Fe,Cr)_{ss}$ phases, this study further investigated the atomic arrangement and strain conditions of the interface, as depicted in Fig. 6 and Fig. S10. Fig. 6c shows the HRTEM image of the $(Ni,Cu,Fe,Cr)_{ss}/(Ni,Cr,Fe)_{ss}$ interface. The lattice reconstruction image in Fig. 6d indicates that a perfect co-occupation was achieved at the interface. The lattice fringe widths of the $(Ni,Cu,Fe,Cr)_{ss(011)}$ and $(Ni,Cr,Fe)_{ss(110)}$ phases are 2.046 Å and 2.123 Å, representing a coherent interface with a lattice misfit of 3.72%. The HRTEM image in Fig. 6g depicts the typical interfacial regions on the right side. The $(Ni,Cu,Fe,Cr)_{ss}$ (yellow atoms) and $(Ni,Cr,Fe)_{ss}$ phases (blue atoms) formed a misfit distribution at the interface (Fig. 6h), which suggested interfacial dislocation emission, thereby coordinating the strain distribution. The fringe widths of $(Ni,Cu,Fe,Cr)_{ss(002)}$ and $(Ni,Cr,Fe)_{ss(110)}$ phases are 2.122 Å and 2.128 Å, respectively. Upon calculation, the interface showed a lattice misfit of 13.24%, manifesting a semi-coherent interface. Moreover, the calibrated fringe widths of the $(Ti,Zr,Hf)_2(Ni,Cu)$ phase (SAED pattern 1) and the $(Ni,Cu,Fe,Cr)_{ss}$ phase (SAED pattern 2) in Fig. S10(a)–(d) were 2.155 Å and 2.126 Å, respectively. The fringe widths of the $(Ni,Cu,Fe,Cr)_{ss}$ phase (SAED 10 pattern) and the $(Ni,Cr,Fe)_{ss}$ phase (SAED 4 pattern) in Fig. S10(e)–(h) were 4.986 Å and 3.984 Å, respectively. The lattice misfits at the $(Ti,Zr,Hf)_2(Ni,Cu)/(Ni,Cu,Fe,Cr)_{ss}$ interface and the $(Ni,Cu,Fe,Cr)_{ss}/(Ni,Cr,Fe)_{ss}$ interface were 18.53% and 20.14%, respectively, both exhibiting a semi-coherent state. The statistical results for the corresponding interfacial relationships are presented in Table S6. Therefore,

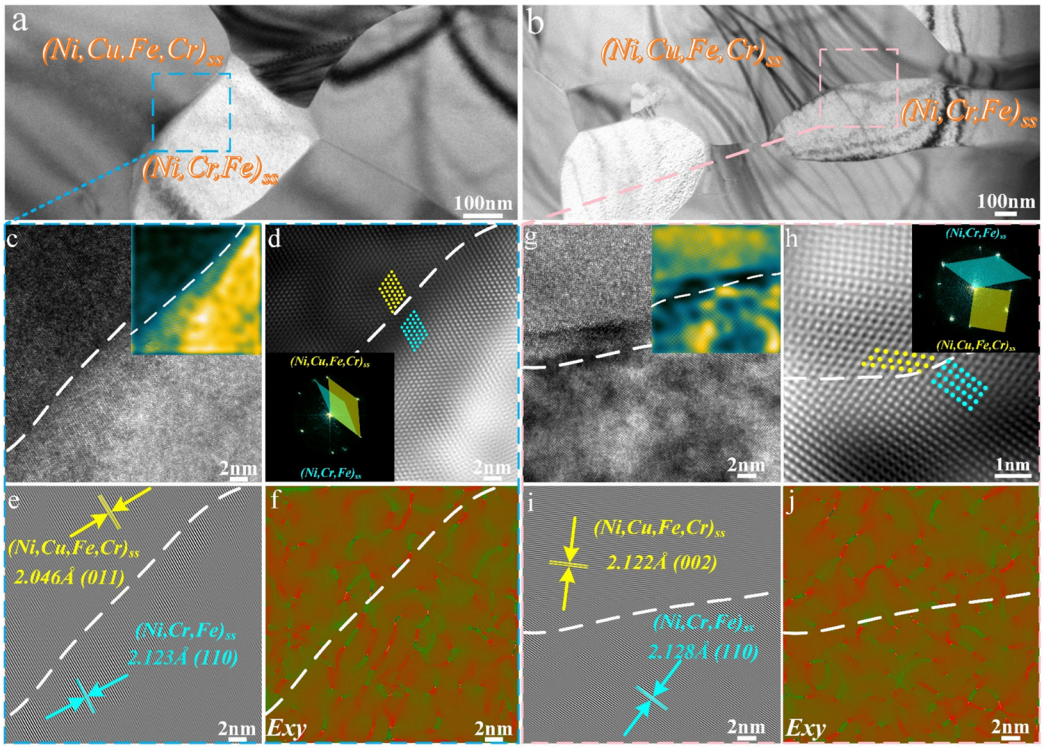


Fig. 6 Interfacial characteristics of joints brazed at 1065 °C for 15 min with the HGFM. (a) and (b) Enlarged bright field images, (c) HRTEM image and lattice distortion conditions in (a), (d) FFT and lattice reconstruction image in (c), (e) lattice fringe image in (c), (f) shear strain distributions of (c), (g) HRTEM image and lattice distortion conditions in (b), (h) FFT and lattice reconstruction image in (g), (i) lattice fringe image in (g), and (j) shear strain distributions of (g).

the primary SS interfaces of joints brazed at 1065 °C were coherent or semi-coherent, facilitating the emission of movable dislocations while maintaining local dynamic equilibrium.[39,40] As reported by Jiang and Wang *et al.*,[41,42] the coherent interface effectively harmonized plastic strain gradients, preventing the rapid formation of critical stress peaks.

In sum, compared to the incoherent IMC state at the interface observed at a brazing temperature of 1020 °C, the coherent/semi-coherent SS state at the interface observed at 1065 °C fundamentally altered the interfacial strengthening mechanism. The transition from resistance-based strengthening to synergistic coordinated strengthening significantly improved deformation capabilities, preventing premature failure caused by the rapid stress concentration, thereby boosting the mechanical properties of the joint.

### 3.4 Mechanical properties of the hybrid joint with the HGFM

Regarding the high-temperature stability of the critical IMC interface and SS interface in the joint, tensile simulations (molecular dynamics, MD) of the $(Ti,Zr)_2(Ni,Cu)/(Ti,Zr)(Ni,Cu)_3$ interface were conducted, as depicted in Fig. 7a and b. The temperature boundary condition for the tensile simulations was set at 923 K, consistent with the service temperature of aeroengine cool-end components.[43] Relevant simulation details are provided in Note S2 of the SI. The peak tensile strength at 923 K increased from 9.49 GPa to 10.36 GPa using the $(Ni,Cr,Fe)_{ss}/(Ni,Cu,Fe,Cr)_{ss}$ model compared to the $(Ti,Zr)_2(Ni,Cu)/(Ti,Zr)(Ni,Cu)_3$ model, presenting superior high-temperature stability and enhanced load-bearing capacity. With increasing brazing temperature, the shear strength of joints first increased and then sharply dropped. At 1065 °C, the shear strength reached a maximum value of 335 MPa. Further increasing the brazing temperature to 1080 °C caused a phase transformation on the $Ti_2AlNb$ side and significant dissolution of base metals, resulting in an increased brittleness tendency, with a shear strength of only 87 MPa. The load–displacement curves of the base metals utilized in this study are presented in Fig. S13. Fig. 7d presents a comparison of the shear strength in joints between TiAl-based alloys and Ni-based superalloys in relevant works. The development of a high-entropy gradient layer filler metal further enhanced the shear strength of joints.[8,9,29,44–50] Furthermore, when combined with the schematic diagram in the SI (Fig. S7), it can be inferred that the SS interface with coherent and semi-coherent relationships of the joints was successfully tailored. Therefore, the design of the HGFM and temperature control in this study not only provided significant advantages in room-temperature performance when brazing Ti–Ni dissimilar metals but also demonstrated promising potential for high-temperature applications.

## 4 Deformation and fracture behavior of the hybrid joint

Fig. 8(a)–(c) depict the nanoindentation morphologies of joints brazed at 1035 °C, 1065 °C and 1080 °C, respectively.

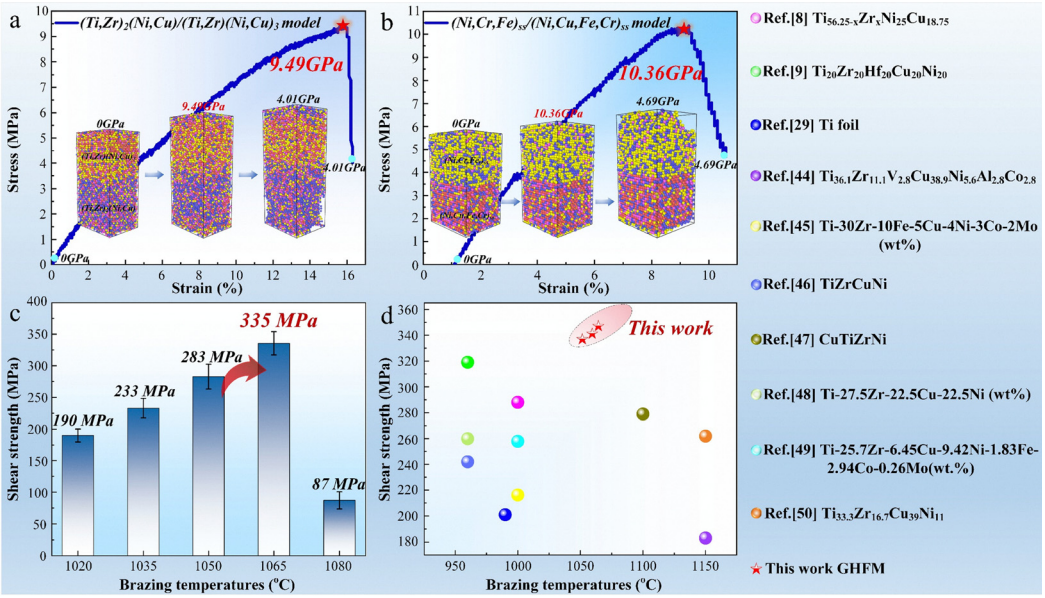


Fig. 7 MD tensile simulation and mechanical properties of Ti–Ni brazed joints with the HGFM. (a) Stress–strain curve and the evolution of atomic configurations of the $(Ti,Zr)_2(Ni,Cu)/(Ti,Zr)(Ni,Cu)_3$ model, (b) stress–strain curve and the evolution of atomic configurations of the $(Ni,Cr,Fe)_{ss}/((Ni,Cu,Fe,Cr)_{ss}$ model, (c) shear strength of joints brazed at different brazing temperatures and (d) comparison of shear strength of joints.

The indentation depths on the base metals were greater than that on the brazed joint, indicating that the hardness of joints was relatively higher than that of the base metals. Fig. 8 presents the hardness and elastic modulus distributions across the brazed joints obtained by the HGFM at 1035 °C, 1065 °C, and 1080 °C. As shown in Fig. 8a, for the joint brazed at 1035 °C, the highest hardness and elastic modulus were located in zone III. Statistical analysis indicated that the average hardness and elastic modulus in zone III were 13.6 GPa and 241.3 GPa, respectively. The elastic modulus reflected the resistance to atomic displacement from equilibrium positions.[51] According to prior research,[52] an abrupt change in elastic modulus across an interface served as a potential site for crack initiation and propagation. Based on this, the paper calculated the average hardness and elastic modulus in the region immediately adjacent to the left side of zone III, which were 10.7 GPa and 178.9 GPa, respectively. Thus, the differences in hardness and elastic modulus between zone III and its neighboring left region were 2.9 GPa and 62.4 GPa, respectively.

Fig. 8b, e, and h display the indentation morphology, hardness distribution, and elastic modulus distribution for the joint brazed at 1065 °C. As depicted in Fig. 8e and h, the regions with the highest average hardness shifted to the boundary between zones I and II. The region with the highest average elastic modulus remained in zone III. The average hardness and elastic modulus in zone III were 9.7 GPa and 225.7 GPa, respectively, while the corresponding values in the left regions were 10.2 GPa and 179.4 GPa. The difference in elastic modulus between zone III and its left-side region at 1065 °C was 46.3 GPa. Comparing joints brazed at 1035 °C and 1065 °C, the elastic modulus gradient across the key interfacial region decreased markedly from 62.4 GPa to 46.3 GPa. This reduction was attributed to a significant transition in zone III from the coherent IMC interface to the

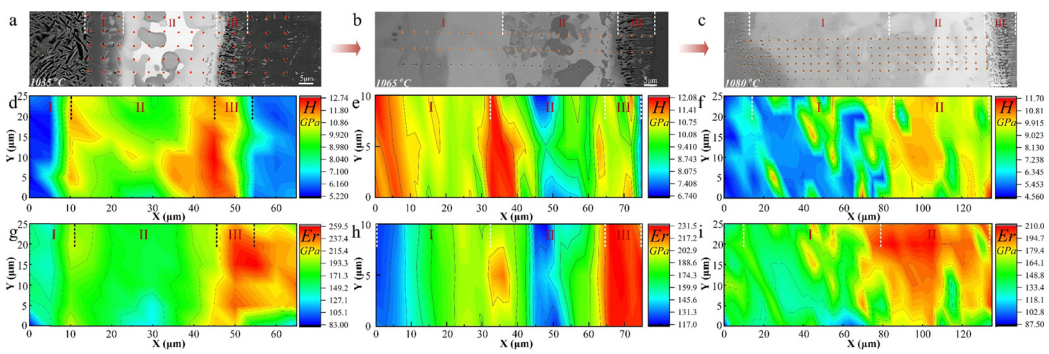


Fig. 8 The position of nanoindentation test points of joints at different brazing temperatures with the HGFM. (a)–(c) Morphologies of indentation, (d)–(f) hardness cloud maps, and (g)–(i) elastic modulus cloud maps.

incoherent and semi-coherent SS interface, which promoted a more gradual transition in elastic modulus and lowered the risk of premature crack initiation and rapid propagation caused by severe modulus mismatch.

Fig. S11 illustrates the fracture paths and morphologies of joints brazed at different temperatures. As the brazing temperature increased from 1035 °C to 1065 °C, the fracture behaviors evolved from a straight crack propagating solely within zone III to a more complex, multi-region crack initiation and propagation patterns. As shown in Fig. S11b, the crack encountered notable resistance at 1065 °C when traversing zone III, indicating enhanced fracture toughness. Therefore, a remarkable transition in the interfacial state increased the deformability of the weak regions, promoting a smoother property transition that was less prone to crack initiation. Moreover, the stress distribution shown in Fig. S11 revealed that as the brazing temperature increases from 1035 °C to 1065 °C, the high-stress regions gradually shifted from the GH4169 interface toward the regions dominated by zone I, and the corresponding maximum stress decreased from 87.6 MPa to 71.5 MPa. Consequently, under external loads, cracks were forced to seek alternative, more favorable propagation paths in zones I and II.

In fact, at brazing temperatures of 1035 °C and 1065 °C, the average hardness and modulus in zone I were significantly lower than those in zones II and III. This indicated that zone I retained excellent plasticity and toughness over a broad temperature range, exhibiting greater deformation capacity. When the brazing temperature was raised to 1080 °C, excessive dissolution of the $Ti_2AlNb$ base metal occurred. It led to the formation of more $Ti_2AlNb$ dissolved with Ni and Cu, as well as a greater amount of (Ti,Zr,Nb)(Ni,Cu) IMCs, inevitably increasing the overall brittleness of the joint. Thus, cracks readily initiated and propagated from the central interfacial region at 1080 °C. Fig. S11c shows that the crack appeared to have minimal resistance during propagation, resulting in a characteristic straight fracture path. In summary, the distinct transition from an incoherent IMC interface to a coherent/semi-coherent SS interface significantly reduced the elastic modulus difference between zone III and adjacent regions, enhanced the compatibility of cooperative deformation across the interface, and ultimately led to a more tortuous fracture path and higher fracture toughness.

## 5 Conclusions

In this study, a high-entropy gradient filler metal with the composition $(TiZrHf)_{50}(NiCu)_{45}Al_5/(TiZrHf)_{30}(NiCu)_{65}Al_5$ based on the gradient + high-entropy rationale was developed to reduce interfacial thermodynamic inclination and exploit high-entropy character, thereby achieving high-strength vacuum brazing between the $Ti_2AlNb$ alloy and the GH4169 superalloy. Key findings and implications are summarized as follows:

(1) The HGFM, as developed through the rationale of low thermodynamic inclination and high entropy characteristics, effectively contributed to relieving the stress concentration and elevating the microstructural stability of the joint, which promoted the formation of a multiphase SS and improved the interfacial relationships.

(2) High entropy induced primary interfacial region transformed from the $(Ti,Zr,Hf)(Ni,Cu)_3$, $(Ti,Zr,Hf)_2(Ni,Cu)$ phases to the $(Ni,Cr,Fe)_{ss}$ and $(Ni,Cu,Fe,Cr)_{ss}$ phases at 1065 °C. The corresponding lattice misfits between $(Ni,Cr,Fe)_{ss}$ and $(Ni,Cu,Fe,Cr)_{ss}$ phases were 3.72%, 13.24% and 20.14%, which enabled coherent and semi-coherent relationships at the SS interface, enabling the dynamic equilibrium of impeding dislocations without terminating them.

(3) Applied GHFM and temperature control promoted the maximum shear strength of the $Ti_2AlNb$/GH4169 brazed joint, reaching 335 MPa. The remarkable reduction in elastic modulus discrepancies in the customized solid solution regions enhanced the synergistic deformation capabilities, ultimately contributing to more tortuous fracture paths and higher fracture toughness.

## Author contributions

Yinchen Wang: conceptualization, investigation, methodology, formal analysis, validation, writing – original draft, and writing – review and editing. Zhijie Ding: conceptualization, formal analysis, and data curation. Bin Wang: methodology and formal analysis. Zhenyang Zhang: investigation, conceptualization, formal analysis, and data curation. Zhiwei Qin: resources, methodology, and writing – review and editing. Jia Yao: methodology and investigation. Yu Sun: conceptualization and investigation. Fengyun Yu: resources and methodology. Honggang Dong: methodology, resources, and supervision. Peng Li: funding acquisition, conceptualization, methodology, resources, and writing – review and editing.

## Conflicts of interest

The authors declare that they have no known competing financial interest or personal relationships that could have appeared to influence the work reported in this paper.

## Data availability

Raw characterization data sets generated during this study, including high-resolution SEM/TEM micrographs, XRD patterns, nanoindentation distribution maps, and load–displacement curves are presented in the manuscript.

Supplementary information (SI): comprehensive details, statistical data, and in-depth analysis. See DOI: https://doi.org/10.1039/d5mh02009c.

## Acknowledgements

This work was financially supported by the National Natural Science Foundation of China (no. 52375313 and 52075074),

 

the Aeronautical Science Foundation (no. ASFC-20240011 063001), the Spring Sunshine Program (no. 202200468) and the Fundamental Research Funds for the Central Universities (no. DUT24BK062). This work was technically supported by the Collaborative Innovation Center of Major Machine Manufacturing in Liaoning and the DUT Instrumental Analysis Center.

## References

1 G. Srinivas, K. Raghunandana and B. Satish Shenoy, *IOP Conf. Ser.:Mater. Sci. Eng.*, 2018, **314**, 12012.
2 L. M. Amoo, *Prog. Aerosp. Sci.*, 2013, **60**, 1–11.
3 M. Dadé, V. A. Esin, L. Nazé and P. Sallot, *Corros. Sci.*, 2019, **148**, 379–387.
4 D. Texier, J. Milanese, M. Jullien, J. Genée, J.-C. Passieux, D. Bardel, E. Andrieu, M. Legros and J.-C. Stinville, *Acta Mater.*, 2024, **268**, 119759.
5 J. P. Oliveira, T. G. Santos and R. M. Miranda, *Prog. Mater. Sci.*, 2020, **107**, 100590.
6 L. Zhang, P. Li and H. Dong, *J. Mater. Sci. Technol.*, 2025, **218**, 287–304.
7 S. Pang, L. Sun, H. Xiong, C. Chen, Y. Liu, H. Li and T. Zhang, *Scr. Mater.*, 2016, **117**, 55–59.
8 L. Zhang, H. Dong, P. Li, S. Li, B. Wu, Y. Ma, L. Huang, C. Li, J. Li and Y. Yang, *J. Mater. Sci. Technol.*, 2023, **154**, 217–231.
9 K. Dong, J. Kong, Y. Peng, Q. Zhou and K. Wang, *J. Mater. Process. Technol.*, 2020, **283**, 116724.
10 K. Dong, J. Kong, X. D. Ruan, Y. Yang, Y. Peng, Q. Zhou and K. H. Wang, *Mater. Sci. Eng., A*, 2021, **815**, 141255.
11 S. Zhao, M. Wang, X. Han, Z. Ding, H. Wang, P. K. Liaw, Y. Wang and Y. Lu, *Mater. Today*, 2025, **88**, 45–54.
12 G. Bracq, M. Laurent-Brocq, C. Varvenne, L. Perrière, W. A. Curtin, J.-M. Joubert and I. Guillot, *Acta Mater.*, 2019, **177**, 266–279.
13 L. Zhou, F. Duan, Y. Zhou, X. Bai, Z. Jiang, T. Zhou, Q. Li, H. Luan, G. Li, J. Luan, X. Chen, A. Chen, Y. Li, X. Wang, T. Yang and J. Lu, *Mater. Today*, 2025, **88**, 99–108.
14 L. Yuan, Y. Z. Yang, J. Gan, T. H. Chou, Y. M. Zhao, D. Hao, J. Y. Zhang, J. L. Li, J. T. Xiong and T. Yang, *Acta Mater.*, 2025, **295**, 121186.
15 W. Ji, R. Zhou, P. Viveganantha, M. See Wu, H. Gao and K. Zhou, *Prog. Mater. Sci.*, 2023, **140**, 101194.
16 K. Lu, *Science*, 2014, **345**, 1455–1456.
17 X. Lv and L. Liu, *J. Magnesium Alloys*, 2024, **12**, 3325–3338.
18 R. Tian, C. Hang, Y. Tian and J. Feng, *J. Alloys Compd.*, 2019, **777**, 463–471.
19 P. Li, Z. Wang, Y. Chen, H. A. Butt, Z. Zhang, Z. Huang, T. Zhang, L. Qiao, Y. Zhong, D. Krasnikov, A. Nasibulin, J. Cao, Y. Yan and J. Qi, *Carbon*, 2025, **242**, 120416.
20 A. Kamal, B. V. Rajasekhar and V. S. Nair, *J. Alloys Compd.*, 2025, **1027**, 180536.
21 Y. J. Du, J. T. Xiong, F. Jin, S. W. Li, L. Yuan, D. Feng, J. M. Shi and J. L. Li, *Mater. Sci. Eng., A*, 2021, **802**, 140610.
22 L. Zhang, H. Dong, P. Li, B. Wu, Y. Ma, L. Huang, C. Li and J. Li, *J. Mater. Sci. Technol.*, 2024, **172**, 51–70.
23 L. Zhang, P. Li, S. Li, F. Nie, B. Wu, C. Li, J. Li, Z. Zhang, X. Jiang, B. Zhao and H. Dong, *Composites, Part B*, 2024, **274**, 111288.
24 W. Tasaki, Y. Akiyama, T. Koyano, S. Miyazaki and H. Y. Kim, *J. Alloys Compd.*, 2023, **931**, 167496.
25 K. Otsuka and X. Ren, *Prog. Mater. Sci.*, 2005, **50**, 511–678.
26 P. Wang, W. Shi, L. Gu, H. Ran, Z. Pan, Y. Su, X. Song, J. Cao, H. Chen and W. Li, *J. Mater. Sci. Technol.*, 2026, **244**, 46–59.
27 B. Xu, J. Zhang, Y. Xiong, S. Ma, Y. Osetsky and S. Zhao, *Cell Rep. Phys. Sci.*, 2023, **4**, 101337.
28 Y. Zhang, Y. Osetsky and W. Weber, *Chem. Rev.*, 2022, **122**, 789–829.
29 H. Li, P. He, T. Lin, F. Pan, J. Feng and Y. Huang, *Trans. Nonferrous Met. Soc. China*, 2012, **22**, 324–329.
30 C.-H. Xia, J. Kundin, I. Steinbach and S. Divinski, *Acta Mater.*, 2022, **232**, 117966.
31 G. Mohan Muralikrishna, N. Esakkiraja, J. Kundin, F. Hisker, J. Berndt, S. Klemme, I. V. Belova, G. E. Murch, A. Paul and S. V. Divinski, *Acta Mater.*, 2025, **292**, 121035.
32 P. Li, S. Wang, Y. Xia, X. Hao and H. Dong, *J. Mater. Sci. Technol.*, 2020, **45**, 59–69.
33 K. X. Yin, Z. W. Huang, B. L. Wu, G. J. Zhang, Q. W. Tian and Y. N. Wang, *Acta Mater.*, 2024, **263**, 119445.
34 K. Alam, W. Jang, G. Jeong, C.-K. Park, K. Lee and H. Cho, *ACS Omega*, 2023, **8**, 28333–28343.
35 Y. Cai and C. Xie, *Phys. Lett. A*, 2021, **411**, 127528.
36 Z. Wu, R. Turner, M. Qi, L. Shi, M. Wang, F. Wang, Z. Gao, Y. Chiu and Z. Zhang, *Acta Mater.*, 2024, **275**, 120051.
37 R. O. Scattergood and D. J. Bacon, *Philos. Mag.*, 1975, **31**, 179–198.
38 A. N. Stroh, *Proc. R. Soc. London, Ser. A*, 1955, **232**, 548–560.
39 Y. Tang, H. Wang, X. Ouyang, C. Wang, Q. Huang, Q. Zhao, X. Liu, Q. Zhu, Z. Hou, J. Wu, Z. Zhang, H. Li, Y. Yang, W. Yang, H. Gao and H. Zhou, *Nat. Commun.*, 2024, **15**, 3932.
40 Y. Wang, Z. Ding, P. Li, Z. Qin, X. Bi, L. Zhang, C. Li, H. Dong, H. Sun, Y. Cheng and Y. S. Sato, *Composites, Part B*, 2025, **297**, 112330.
41 S. Jiang, H. Wang, Y. Wu, X. Liu, H. Chen, M. Yao, B. Gault, D. Ponge, D. Raabe, A. Hirata, M. Chen, Y. Wang and Z. Lu, *Nature*, 2017, **544**, 460–464.
42 J. Wang and A. Misra, *Curr. Opin. Solid State Mater. Sci.*, 2011, **15**, 20–28.
43 T. M. Pollock, *Nat. Mater.*, 2016, **15**, 809–815.
44 S. Li, Z. Liu, Y. Xia, X. Wang, P. He, Y. Jiu, L. Jia and W. Long, *J. Manuf. Process.*, 2021, **70**, 484–493.
45 B. Wan, X.-Q. Li, C.-L. Pan, D.-Y. Li, S.-G. Qu and C. Yang, *Rare Met.*, 2021, **40**, 2134–2142.
46 J. Cai, S. Hu, H. Liu, D. Lin, W. Fu and X. Song, *Aerospace*, 2023, DOI: 10.3390/aerospace10010073.
47 D. Dong, K. Shi, D. Zhu, Y. Liang, X. Wang, Z. Wei and J. Lin, *Intermetallics*, 2021, **139**, 107351.
48 C. Jiang, X. Li, B. Wan, D. Zhu, S. Qu and C. Yang, *Intermetallics*, 2022, **142**, 107468.

49 L. Li, W. Zhao, Z. Feng, J. Sun and X. Li, *Trans. Nonferrous Met. Soc. China*, 2020, **30**, 2143–2155.
50 Y. Xia, Z. Ma, Q. Du, Y. Jiu, P. Guo, J. Qin, S. Li, X. Zhang, P. Zhou, J. Hu, S. Zhong and W. Long, *Mater. Charact.*, 2024, **207**, 113520.
51 S. Khan, C. Annavarapu and A. Rodríguez-Ferran, *Int. J. Adv. Eng. Sci. Appl. Math.*, 2023, **15**, 173–186.
52 N. G. Mathews, A. Lambai, M. Hans, J. M. Schneider, G. Mohanty and B. N. Jaya, *Adv. Eng. Mater.*, 2025, **27**, 2500285.

 